

## Article

# New Insights for Gem-Quality Mn-Bearing Diopside-Omphacite, Violane Variety, from Saint Marcel (Val D'Aosta, Italy): Its Trace Elements and Spectroscopic Characterization

Valeria Diella <sup>1,\*</sup> , Rosangela Bocchio <sup>2</sup>, Franca Caucia <sup>3</sup>, Nicoletta Marinoni <sup>2</sup>, Antonio Langone <sup>4</sup> and Elena Possenti <sup>5</sup> 

<sup>1</sup> National Research Council, Institute of Environmental Geology and Geoengineering (IGAG), Section of Milan, 20133 Milan, Italy

<sup>2</sup> Department of Earth Sciences "Ardito Desio", University of Milan, 20133 Milan, Italy; rosangela.bocchio@unimi.it (R.B.); nicoletta.marinoni@unimi.it (N.M.)

<sup>3</sup> Department of Earth and Environmental Sciences, University of Pavia, 27100 Pavia, Italy; caucia@crystal.unipv.it

<sup>4</sup> National Research Council, Institute of Geosciences and Earth Resources (IGG), Section of Pavia, 27100 Pavia, Italy; langone@igg.cnr.it

<sup>5</sup> National Research Council, Institute of Heritage Science (ISPC), Section of Milan, 20125 Milan, Italy; elena.possenti@cnr.it

\* Correspondence: valeria.diella55@gmail.com; Tel.: +39-02-50315621



**Citation:** Diella, V.; Bocchio, R.; Caucia, F.; Marinoni, N.; Langone, A.; Possenti, E. New Insights for Gem-Quality Mn-Bearing Diopside-Omphacite, Violane Variety, from Saint Marcel (Val D'Aosta, Italy): Its Trace Elements and Spectroscopic Characterization. *Minerals* **2021**, *11*, 171. <https://doi.org/10.3390/min11020171>

Academic Editor:

Thomas Hainschwang

Received: 11 January 2021

Accepted: 1 February 2021

Published: 7 February 2021

**Publisher's Note:** MDPI stays neutral with regard to jurisdictional claims in published maps and institutional affiliations.



**Copyright:** © 2021 by the authors. Licensee MDPI, Basel, Switzerland. This article is an open access article distributed under the terms and conditions of the Creative Commons Attribution (CC BY) license (<https://creativecommons.org/licenses/by/4.0/>).

**Abstract:** This study proposes new data on the rare pyroxene, variety violane, sampled from its type locality, Praborna manganese deposit, near Saint Marcel (Val d'Aosta, Italy). Violane is very appreciated as a gemstone for its different hues of violet-blue color and is characterized by its diopside or omphacitic composition. To assess the possible causes of color, electron-probe microanalysis (EMPA) and laser-ablation inductively coupled plasma mass spectrometry (LA-ICP-MS) were used to establish the chemical composition. Raman and Fourier transform infrared (FTIR) spectroscopy, ideal for the non-destructive analysis, identified the different present phases directly on gemstone. Raman and FTIR spectra highlighted the presence, in the same sample, of diopside and omphacite showing almost inappreciable violet hue difference. The two minerals were easily differentiated by microprobe analyses and showed a compositional heterogeneity not linked to the different colors. The best way to detect the color-causing elements in microcrystalline violanes resulted in the analysis of trace elements and their quantification. An enrichment of Ti and Li characterizes darker violet omphacite and that of V and rare-earth elements (REE) the lilac-lavender or light violet-blue diopside. In general, our results led us to say that the color changes, previously proposed as due to Mn both in divalent and trivalent oxidation state, may be controlled by trace elements or by concentration of minor elements, such as Fe, and their oxidation state. REE patterns showed a negative anomaly of Ce that could be ascribed to the variation of the oxygen chemical potential occurring in the ore. The new data, combined with previous results, may provide new constrains on the processes that generated the Mn-rich deposit of Praborna.

**Keywords:** violane-pyroxene; gemology; Val d'Aosta; Western Alps; Italy

## 1. Introduction

Pyroxene, variety violane (or violan) from the Mn-ore deposit of Praborna in Saint Marcel Valley (Valle d'Aosta Region, North Western Italy; WGS84 system: lat. 45°40'45" N; long. 7°26'57" E) is a rare mineral in nature and has been considered as gem-quality material since last century due to its beautiful color varying from purple-blue to violet. In the catalogue of "Italian Type Minerals", the violane of Praborna mine is quoted as "a

rare light blue to purple, manganese-rich variety” of diopside, which is itself a mineral species first discovered in Italy [1]. However, this definition is not at all complete because many years ago, it was proved that the violet-blue clinopyroxenes from Praborna belong to two separate species: diopside,  $\text{CaMg}(\text{Si}_2\text{O}_6)$ , and omphacite,  $(\text{Ca},\text{Na})(\text{Mg},\text{Fe},\text{Al})(\text{Si}_2\text{O}_6)$ , differing both in composition and space group symmetry [2–5].

The Saint Marcel area is the most significant locality (type locality) for gem-quality violane in the world, and actually, only few other occurrences are known, e.g., as ornamental blue diopside from different localities in Russia ([6] and references therein) or as massive aggregates from southern Baffin Island Nunavut, Canada [7] and from Vitali, Andros Island, Greece [8].

Fine material has been found in a limited amount in a restricted part of the Praborna mine (Figure 1), and only a few pieces have been set into jewelry. In particular, among collectors and jewelers, there are also known colorless quartz cabochons with violane inclusion sampled in the quartz-rich veins [9] (Figure 2). However, both the veins and inclusions of violane are rather narrow (from millimetric to decimetric in size), therefore the material lends itself to small cabochons and carvings. To date, local mineral collectors continue to work the deposit, and it is likely that small amounts of fine violane will continue to be produced in the future.

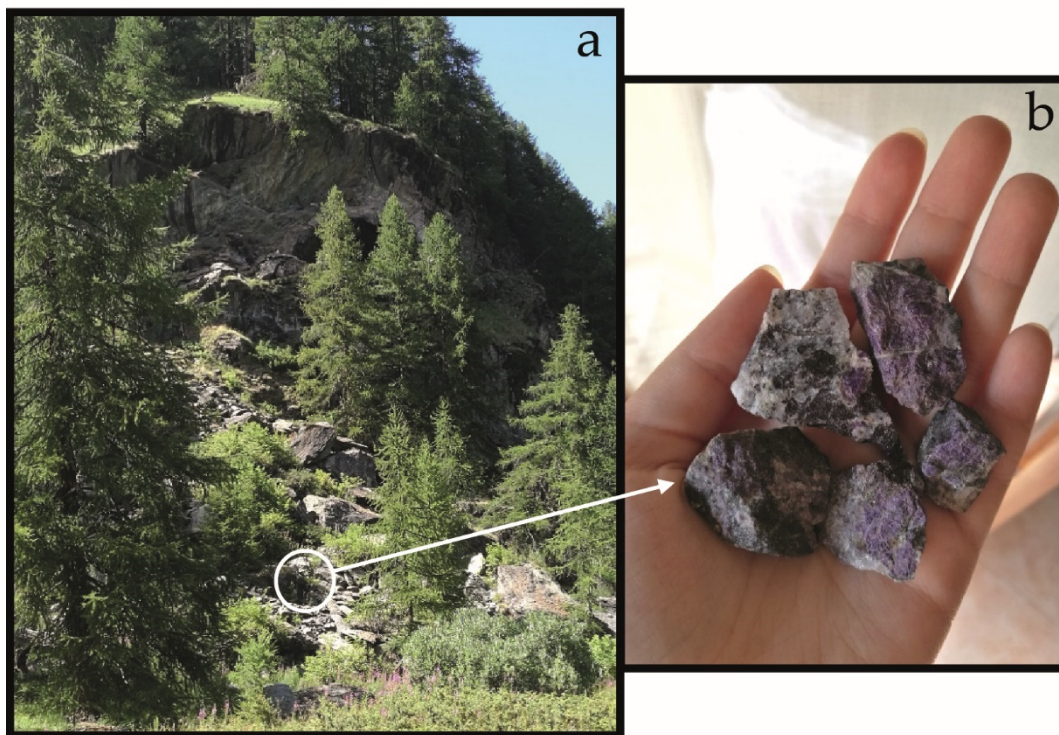


**Figure 1.** Mine and landfill of Praborna (a) and collected samples (b).

Because a study on the gemological properties of this very rare variety of pyroxene is lacking, and the chemical and physical data, except for the more recent work of [10], are more than 40 years old, we prepared this review and update including a complete gemological characterization together with new information concerning trace element profiles and Raman and FTIR spectroscopy.

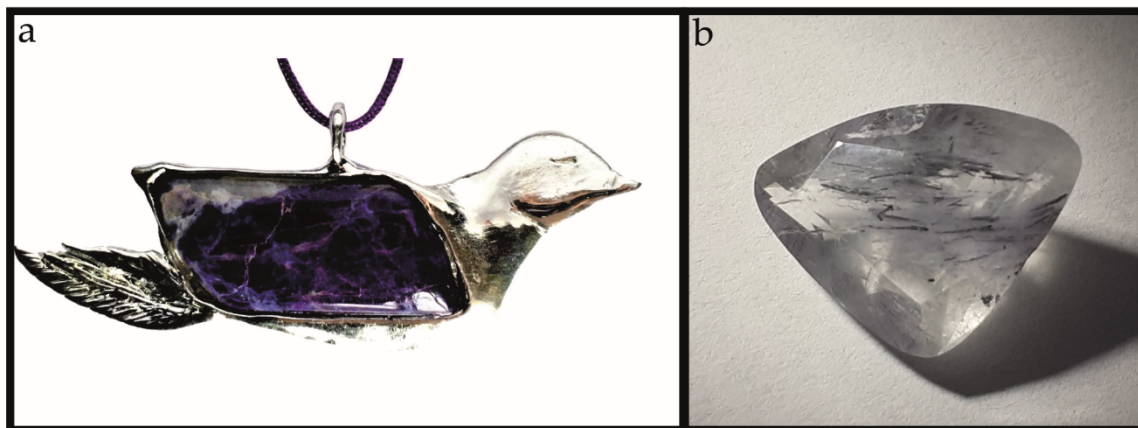


**Figure 2.** Pendant of violane, 3.5 cm × 2.5 cm, photo by “Lutezia Gioielli, Stradella, Pavia, Italy” (a) and quartz trillion cut containing violet inclusions of violane, 2.5 ct, photo by F. Caucia (b).

## 2. Background Information

The Praborna mine occurs in the Zermatt-Saas meta-ophiolite unit of the Western Alps and formed as hydrothermal sediment at the oceanic spreading center. In this area, the oceanic crust was subducted and metamorphosed up to eclogite facies conditions during the Eoalpine high-pressure–low-temperature phase of the alpine orogenesis [11–13].

The deposit is considered as the most important and famous Mn occurrence of the Piemonte nappe and is constituted by boudinaged quartz-rich layers with Mn oxides and silicates. It also contains a few intercalations of metapelites and metavolcanites [14,15].

The Mn ore of Praborna has been known since the beginning of the 15th century when the mining of braunite ( $\text{Mn}^{2+}\text{Mn}^{3+}_6\text{O}_8(\text{SiO}_4)$ ) started and was utilized for the glassmaking in Venice and in southern France [16]. The exploitation of the mine lasted for a several centuries, and it was closed only at the beginning of the 20th century. However, its minerals were extensively studied by mineralogists mainly during 1800. In particular, the clinopyroxene was described and named “violane” after its violet color by [17] and re-examined by [18,19]. Based on the chemical analyses carried out in 1800, for many years, violane was mentioned in most mineralogy handbooks as a weak manganese variety of diopside [20–22]. It was only in the seventies of the last century that careful chemical and crystallographic investigations finally proved that the violet-blue pyroxene from Saint Marcel is not a mineral species and the name violane must “be reserved for the ex colore violet varieties of both diopside and omphacite” [4]. Some years later, in the report of the “Subcommittee on pyroxene” established by the International Mineralogical Association (IMA), the term violane was considered obsolete and the mineral classified as a Mg-rich augite or diopside [23]. More recently, in the list of the IMA Commission on Gem Material (CGM), updated in July 2018, the term violan/violane is quoted in bold as “non-mineral” and not approved. The comment suggests defining the material as Omp-V or Di-V, if known composition, Vio if unknown.

Violane is not widespread in the deposit of Praborna, but it occurs only in a braunite-rich layer defined in literature as “level 1” (i.e., basal level) that was intensively mined, and at present, it is highly fractured and almost disappeared [14,15]. This level contains the following as accessory minerals: quartz, piemontite, Na-Ca amphibole, carbonate, and along the fracture, Mn-rich muscovite (alurgite). The braunite + violane + quartz assemblage records the peak conditions of metamorphism ( $P = 2.1 \pm 0.3$  GPa and  $T = 550 \pm 60$  °C) estimated in the St. Marcel valley [24].

## 3. Materials and Methods

The considered samples come from the last geological field trip and, in part, belong to the Bazzi historical collection preserved in the Museum of the Department of Earth

Sciences of the University of Milan, Italy and to the private collection of one of the authors (F.C.). The analyzed material came from “level 1” of the mine and from the near mine landfill. It consists of 8 cut and polished (one sphere and seven free formed cabochons) and 3 rough fine-grained specimens with massive aspect and different and inhomogeneous distribution of violet color (hereinafter indicated as massive samples). Moreover, 15 small fragments of violane, ranging from 0.5 to 1 mm in diameter, were selected as representative of different hues from pink, lilac-lavender to pale and dark violet-blue color (hereinafter indicated as fragments). These fragments were embedded all together in a mount with epoxy resin, polished and prepared for EMP and laser-ablation inductively coupled plasma mass spectroscopy (LA-ICP-MS) analyses.

The cut samples were visually examined by a gemological microscope (A. Krüss Optronic, Hamburg, Germany) and analyzed by standard gemological methods at the University of Pavia. The hue of the color was determined using a Pantone colorimeter (X-Rite incorporated, Prato, Italy) and the RGB colors system, whereas the dimensions were obtained by a manual gem caliper. The refraction indices (RI) were measured by the distant method with a Krüss ER6040 (A. Krüss Optronic, Hamburg, Germany) refractometer using sodium light (589 nm) from a Leitz lamp and methylene iodide saturated with sulfur and C214 as a contact liquid (R.I. = 1.81). A Tanita 1210 (Tanita Corporation Arlington Heights, IL, USA) hydrostatic balance was used to determine the specific gravity (SG) and the weight in carats (ct).

Besides standard gemological testing, one faceted sample was analyzed by Raman spectroscopy at the laboratories of the University of Pavia. Micro-Raman scattering measurements were conducted using a Horiba Jobin-Yvon Xplora Plus single monochromator spectrometer (with a grating of 2400 groove/mm) equipped with an Olympus BX41 microscope. Raman spectra were excited by the 532 nm line. The spectrometer was calibrated to the silicon Raman peak at  $520.5\text{ cm}^{-1}$ . The spectral resolution was  $\sim 2\text{ cm}^{-1}$ , and the instrumental accuracy in determining the peak positions was  $\sim 0.56\text{ cm}^{-1}$ . Raman spectra were collected in the spectral range  $100\text{--}1200\text{ cm}^{-1}$  for 5 s averaging over 40 accumulations.

Fourier transform infrared spectroscopy (FTIR) investigations were carried out using a Thermo Scientific™ Nicolet™ iS50 FT-IR spectrophotometer coupled with a Continuum™ infrared microscope with mercury cadmium telluride (MCT/A) detector cooled with liquid nitrogen in the laboratories of the Institute of Heritage Science (ISPC), CNR, Milan. The measurements were carried out in specular reflectance geometry in the spectral range  $4000\text{--}650\text{ cm}^{-1}$ . FTIR spectra were collected with a spectral resolution of  $4\text{ cm}^{-1}$  and 128 co-added scans. The investigated area for each FTIR spectrum was  $100 \times 100\ \mu\text{m}^2$ . The background spectra were collected on a golden mirror using the same parameters of FTIR spectra. Once a region of interest was identified in the gem, three FTIR spectra were collected on three different  $100 \times 100\ \mu\text{m}^2$  areas in order to explore possible variations of the vibrational features due to compositional variations of the crystalline phases in the sample. In the following, the FTIR spectra are presented in reflectance without any spectral manipulation or spectral conversion. The FTIR analysis was carried out in the same points investigated by Raman spectroscopy.

Backscattered electron (BKSE) images and quantitative chemical analyses of major and minor elements were performed at the laboratory of the University of Milan on the three rough samples (PV2, 3, 4) and on the mount with the fifteen fragments using a JEOL JXA-8200 electron microprobe in wavelength dispersion mode (EMPA-WDS) under the following conditions: 15 kV accelerating voltage, 5 nA beam current, and a counting time of 60 s on peak and 30 s on the backgrounds. Natural minerals were used as standards. The raw data were corrected for matrix effects using a conventional  $\Phi\rho Z$  routine in the JEOL software package (version 3.50).

Rare earth elements (REE) and other trace elements were determined by laser-ablation inductively coupled plasma mass spectroscopy (LA-ICP-MS) at IGG-CNR Laboratory of Pavia combining an excimer laser (193 nm; Lambda Physik with GeoLas optics) with a triple quadrupole ICPMS (QQQ Agilent 8900). Analyses were performed on or close

to sites previously analyzed at the EMPA. The laser was operated at a repetition rate of 10 Hz, with a fluence of  $6 \text{ J}\cdot\text{cm}^{-2}$  and an ablation spot size of  $55 \mu\text{m}$ . The optimization of LA-ICP-MS to minimize elemental fractionation was performed by ablating NIST 612 glass and adjusting the nebulizer Ar and the carrier laser cell He gas flows to obtain the ratio of  $^{232}\text{Th}$  and  $^{238}\text{U}$  signals close to 1 by minimizing the  $\text{ThO}^+/\text{Th}^+$  ratio ( $<1\%$ ) in order to reduce the formation of polyatomic oxides. The selected masses were acquired in MS/MS mode, and each analysis consisted of the acquisition of 1 min of background before and after about 1 min of ablation signal.

Data reduction was performed with the “GLITTER” software package (van Achtenbergh et al., 2001) using NIST SRM 610 glass as an external standard and  $^{29}\text{Si}$  as an internal standard, changing the value in each analysis as from microprobe. Precision and accuracy estimated on the USGS basaltic glass standard BCR2 and NIST612 were better than 10%. The minimum detection limit (99%\_confidence) for each analysis points is reported in Table S1 (Supplementary Materials).

## 4. Results

### 4.1. Gemological Properties

The gemological properties of eight cut samples of violane (10.42–38.67 ct) are listed in Table 1. They were fashioned from rough specimens containing crystals of violane associated with braunite, piemontite, albite, quartz, and alurgite (Figure 3). The complex polymineralic composition contributes to the variable color of the samples ranging from pale to dark violet up to deep blue. Irregular striped or spotted color zoning was observed in nearly every sample. The various modal proportions of the minerals associated with violane also contribute to the variation from 2.92 to 3.30 of specific gravity (SG) values that, with the unique exception of gem 2, are lower than those of quality gem diopside and omphacite, ranging from 3.22 to 3.38 and from 3.16 to 3.43, respectively (Manual of Mindat.org. 2020). However, the refraction index (RI) values (1.680–1.715) are within the typical diopside and omphacite range of 1.664–1.730 and 1.662–1.723, respectively. All the stones were opaque and inert to long and short-wave UV radiation.

**Table 1.** Physical and optical data.

Gem	Weight (ct)	SG ( $\text{g}/\text{cm}^3$ )	Refraction Index	Color (GIA)	Cut/Shape
1	11.54	2.98	1.694	Pantone 2745U + 2695C Purple 4 – Blue Violet	Cabochon
2	38.67	3.3	1.715	Pantone 2745U + 273U Blue Violet – Purple 2	Cabochon
3	20.24	3.04	1.7	Pantone 2747U + 5285C Slate Blue 1	Cabochon
4	10.42	2.92	1.68	Pantone 2695C Purple 4	Sphere
5	12.01	2.96	1.685	Pantone 2736U + 2738U Medium Slate Blue – Medium Purple 4	Cabochon
6	20.47	2.97	1.69	Pantone 273U + 2695C Purple 4 – Blue Violet	Cabochon
7	12.06	2.97	1.688	Pantone 2695C Purple 4	Cabochon
8	11.73	2.99	1.698	Pantone 273U + 2695C Purple 4 – Blue Violet	Cabochon

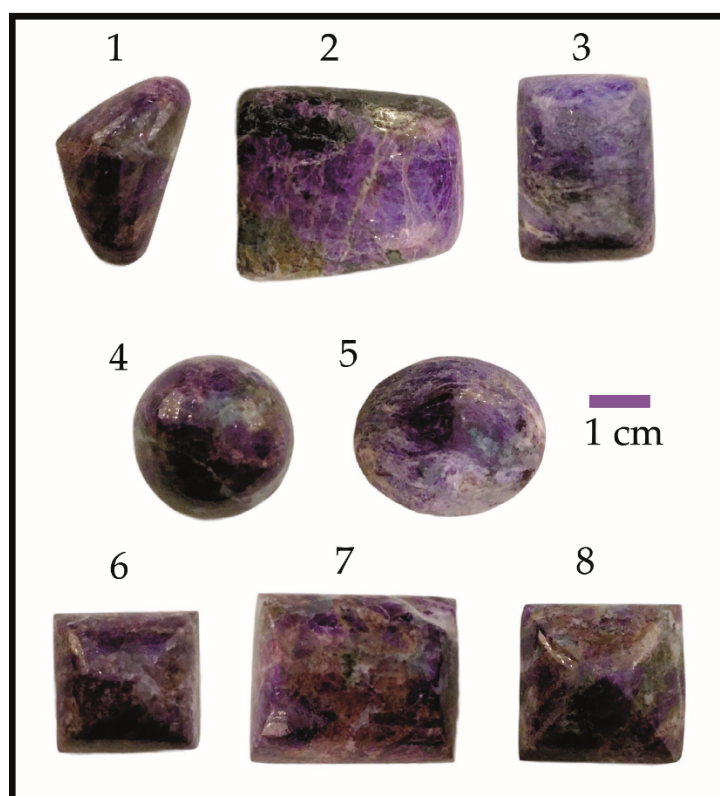


**Figure 3.** Cut violane stones described in Table 1.

#### 4.2. Major Element Composition

Selected chemical analyses of violane samples from Praborna mine are presented in Table 2a,b, referring to massive samples and fragments, respectively. In the stoichiometric formula, calculated on the basis of four cations, the determination of the oxidation states of Fe and Mn was based assuming for both elements the divalent state and the charge balance equation  $\text{Na} + \text{K} + \text{Al}^{\text{IV}} = \text{Al}^{\text{VI}} + \text{Cr} + 2\text{Ti} + \text{M}^{3+}$  where  $\text{M}^{3+} = \text{Fe}^{3+} + \text{Mn}^{3+}$ , as suggested by [4]. In the analyses, all Fe resulted in the trivalent state, but a deficit of  $\text{M}^{3+}$  gives evidence of the occurrence in these pyroxenes also of  $\text{Mn}^{3+}$ .

**Table 2.** Selected electron microprobe analyses of the violane (a) massive samples (PV2,3,4) and (b) fragments from Praborna mine, Saint Marcel (wt. %).

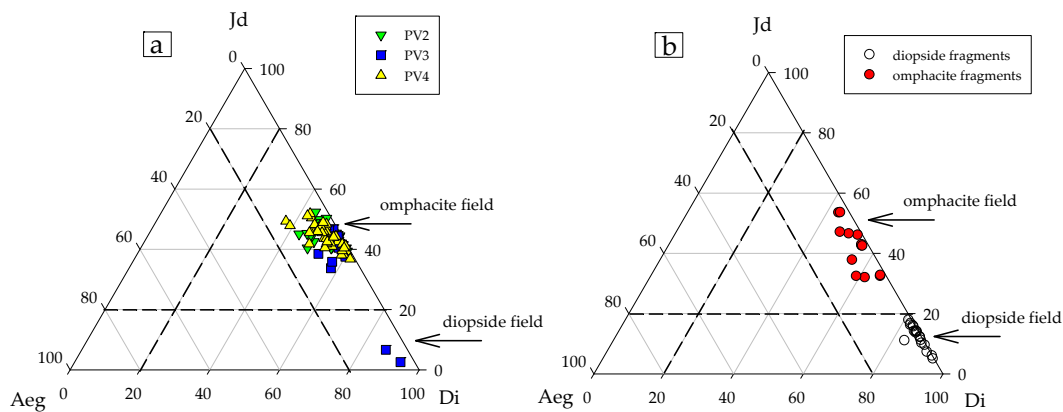
(a)										
Sample	PV2			PV3			PV3-12		PV4	
	Average 43 pts	Minimum	Maximum	Average 20 pts	Minimum	Maximum	Diopside	Average 44 pts	Minimum	Maximum
SiO <sub>2</sub>	56.84	56.25	57.49	56.89	56.34	57.26	55.62	56.90	56.34	57.52
TiO <sub>2</sub>	0.05	-	0.19	0.10	0.04	0.23	-	0.10	-	0.38
Al <sub>2</sub> O <sub>3</sub>	10.05	8.98	11.94	9.49	7.77	10.49	0.67	10.30	8.62	12.13
Cr <sub>2</sub> O <sub>3</sub>	0.01	-	0.09	0.01	-	0.06	-	0.01	-	0.08
FeO <sub>tot</sub>	1.14	0.20	3.91	1.05	0.36	3.09	1.51	1.52	0.19	4.45
MnO <sub>tot</sub>	1.18	0.70	1.65	1.25	1.08	1.46	0.16	0.98	0.59	1.47
MgO	9.75	8.07	11.03	10.20	9.24	11.07	16.99	9.51	7.24	11.17
CaO	14.11	11.60	15.79	14.65	13.52	15.92	24.68	13.72	10.05	16.42
Na <sub>2</sub> O	7.00	5.92	8.36	6.59	5.80	7.12	0.96	7.14	5.70	9.13
Total	100.14	-	-	100.25	-	-	100.59	100.20	-	-
Fe <sub>2</sub> O <sub>3</sub>	1.27	0.22	4.35	1.17	0.40	3.43	1.68	1.68	0.21	4.95
MnO	0.56	0.01	1.28	0.69	0.26	1.23	0.16	0.66	0.01	1.31
Mn <sub>2</sub> O <sub>3</sub>	0.69	-	1.54	0.62	-	1.10	-	0.35	-	1.29
Total	100.34	-	-	100.46	-	-	100.76	100.40	-	-
Number of ions on the basis of 4 cations										
Si	1.996	-	-	2.000	-	-	1.996	1.997	-	-
Al <sup>IV</sup>	0.004	-	-	-	-	-	0.004	0.003	-	-
Al <sup>VI</sup>	0.412	-	-	0.393	-	-	0.024	0.424	-	-
Ti	0.001	-	-	0.003	-	-	-	0.003	-	-
Cr	-	-	-	-	-	-	-	-	-	-
Fe <sup>3+</sup>	0.034	-	-	0.031	-	-	0.045	0.044	-	-
Mn <sup>2+</sup>	0.012	-	-	0.018	-	-	0.005	0.019	-	-
Mn <sup>3+</sup>	0.023	-	-	0.019	-	-	-	0.010	-	-
Mg	0.511	-	-	0.534	-	-	0.909	0.498	-	-
Ca	0.531	-	-	0.552	-	-	0.949	0.516	-	-
Na	0.476	-	-	0.449	-	-	0.067	0.486	-	-
Calculated end-members										
Di	0.52	-	-	0.53	-	-	0.93	0.50	-	-
Jd	0.42	-	-	0.40	-	-	0.03	0.43	-	-
Aeg	0.03	-	-	0.03	-	-	0.04	0.04	-	-
Others	0.04	-	-	0.04	-	-	0.00	0.03	-	-

Table 2. Cont.

(b)																
Sample	Omphacite Fragments						Diopside Fragments									
	3-1	3-2	6-1	12-1	12-2	13-1	13-2	1-1	1-2	2-1	2-2	6-2	10-1	10-2	17-1	17-2
SiO <sub>2</sub>	56.74	57.40	56.91	56.24	56.58	56.85	56.62	55.58	55.50	56.03	55.64	55.07	55.78	55.78	55.98	55.34
TiO <sub>2</sub>	0.02	0.08	-	0.05	0.03	0.14	0.07	0.02	0.01	0.01	0.07	-	0.01	0.06	-	0.08
Al <sub>2</sub> O <sub>3</sub>	7.62	10.76	10.69	8.98	7.03	9.13	7.31	3.12	2.38	3.85	3.19	2.85	2.23	2.51	3.62	1.10
Cr <sub>2</sub> O <sub>3</sub>	-	-	-	-	-	0.03	-	0.02	0.03	0.01	0.02	-	0.02	0.03	0.01	-
FeO <sub>tot</sub>	0.58	0.44	1.90	2.38	1.97	0.56	2.74	0.31	0.33	0.29	0.37	1.99	0.15	0.23	0.19	0.11
MnO <sub>tot</sub>	0.96	1.00	0.99	0.98	1.19	1.40	1.04	1.23	0.92	1.16	1.10	0.84	1.07	1.50	1.43	0.72
MgO	12.06	10.09	9.29	10.31	11.69	10.90	10.98	15.26	15.77	14.78	15.55	15.44	16.23	15.64	15.00	17.32
CaO	17.48	14.33	12.39	14.55	16.62	15.18	15.98	22.10	23.18	21.45	22.09	21.19	23.34	22.69	21.54	24.59
Na <sub>2</sub> O	5.08	6.77	7.29	6.91	5.40	6.24	5.83	2.35	1.82	2.64	2.33	2.25	1.81	2.02	2.46	0.97
Total	99.99	99.95	99.46	100.69	100.38	100.40	100.51	100.21	100.36	100.56	98.52	99.63	100.53	99.77	100.44	100.58
Fe <sub>2</sub> O <sub>3</sub>	0.64	0.49	2.11	2.64	2.19	0.62	3.05	0.34	0.37	0.32	0.41	2.21	0.17	0.25	0.21	0.12
MnO	0.53	1.00	0.99	0.08	1.19	1.40	1.04	0.56	0.45	0.77	0.73	0.84	0.21	0.72	1.03	0.29
Mn <sub>2</sub> O <sub>3</sub>	0.47	-	-	0.99	-	-	-	0.75	0.53	0.43	0.41	-	0.96	0.87	0.44	0.49
Total	100.65	100.92	99.67	100.76	100.73	100.50	100.88	100.10	100.04	100.29	100.44	99.85	100.74	100.57	100.30	100.30
Number of ions on the basis of 4 cations																
Si	1.998	1.999	2.011	1.973	1.998	1.995	2.000	1.993	1.995	2.002	1.986	1.987	1.989	1.996	2.002	1.986
Al <sup>IV</sup>	0.002	0.001	-	0.027	0.002	0.005	-	0.007	0.005	-	0.014	0.013	0.011	0.004	-	0.014
Al <sup>VI</sup>	0.314	0.440	0.445	0.344	0.291	0.372	0.304	0.124	0.096	0.162	0.120	0.108	0.083	0.101	0.153	0.033
Ti	-	0.002	-	0.001	0.001	0.004	0.002	0.001	-	-	0.002	-	-	0.002	-	0.002
Cr	-	-	-	-	-	0.001	-	0.001	0.001	-	0.001	-	-	0.001	-	-
Fe <sup>3+</sup>	0.017	0.013	0.056	0.070	0.058	0.016	0.081	0.009	0.010	0.009	0.011	0.060	0.004	0.007	0.006	0.003
Mn <sup>2+</sup>	0.016	0.029	0.030	0.003	0.036	0.042	0.031	0.017	0.014	0.023	0.022	0.026	0.006	0.022	0.031	0.009
Mn <sup>3+</sup>	0.013	-	-	0.026	-	-	-	0.020	0.014	0.012	0.011	-	0.026	0.024	0.012	0.013
Mg	0.633	0.524	0.489	0.539	0.616	0.570	0.578	0.816	0.845	0.787	0.827	0.830	0.863	0.834	0.800	0.927
Ca	0.660	0.535	0.469	0.547	0.629	0.571	0.605	0.849	0.893	0.821	0.845	0.819	0.892	0.870	0.825	0.946
Na	0.347	0.457	0.499	0.470	0.370	0.424	0.399	0.163	0.127	0.183	0.161	0.157	0.125	0.140	0.171	0.068
Calculated end-members																
Di *	0.64	0.51	0.46	0.54	0.60	0.53	0.57	0.82	0.86	0.79	0.82	0.81	0.87	0.84	0.80	0.92
Jd **	0.32	0.45	0.46	0.37	0.31	0.41	0.31	0.13	0.10	0.16	0.14	0.11	0.09	0.11	0.15	0.05
Aeg ***	0.02	0.01	0.06	0.07	0.06	0.02	0.08	0.01	0.01	0.01	0.01	0.05	-	0.01	0.01	-
Others	0.03	0.03	0.03	0.03	0.03	0.04	0.03	0.04	0.03	0.04	0.03	0.03	0.03	0.05	0.04	0.02

\* Di = diopside, \*\* Jd = jadeite, \*\*\* Aeg = aegirine.

The chemical composition of the clinopyroxenes studied here can be expressed through the general formula  $(Ca,Na)(Mg,Fe^{2+},Fe^{3+},Al)(Si_2O_6)$ , and the individual analyses are presented in terms of the three end-members, diopside ( $CaMgSi_2O_6$ , Di), jadeite ( $NaAlSi_2O_6$ , Jd), and aegirine ( $NaFe^{3+}Si_2O_6$ , Aeg) in triangular diagrams of Figure 4. Figure 4a shows that all the massive samples (PV2, 3, 4) are strongly enriched in the Di and Jd component with respect to Aeg and that most analyses lie in the omphacite field (20–80% Jd), according to the nomenclature of [23]. Only two diopside points found in the sample PV3 and showing a Jd content <20% fall in the field of Ca-Mg-Fe pyroxene (representative analysis PV3-12 is listed in Table 2). Both the analyses were performed on an area of the sample showing a whitish, lighter violet color.



**Figure 4.** Di-Jd-Aeg diagram of the individual data points of samples PV2, 3, 4 (a) and of diopside and omphacite fragments (b).

The occurrence of two mineral species is confirmed in Figure 4b, where the analyses, performed on the mount with the crystal fragments, are plotted. However, in this case, the chemical variation both of omphacite and diopside samples are slightly enlarged and the compositional gap along the Di-Jd joint is more restricted. In general,  $FeO_{tot}$  and  $MnO_{tot}$  showed a wide variation from 0.2 to 4.45 and from 0.6 to 1.65 wt. %, respectively, without a clear correspondence with the different hues.

In particular, this chemical heterogeneity appears in PV2, 3, and 4 omphacites from the analyses performed on different lines across the samples. As an example, Figure 5 shows sample PV4, its BKSE image, and the diagrams with selected element content determined along two representative profiles (line 1 and 3). In both the lines, the exchanges between Na and Ca are visible. The minor elements (Fe, Mn, Ti) do not show any significant variation with the exception of an increase in Fe in line 3, corresponding to the points with the highest content of Na.

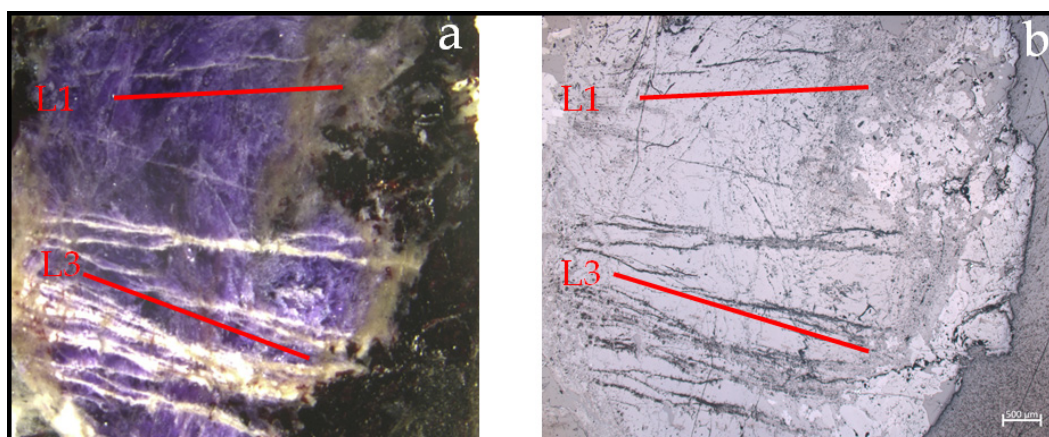


**Figure 5.** Cont.

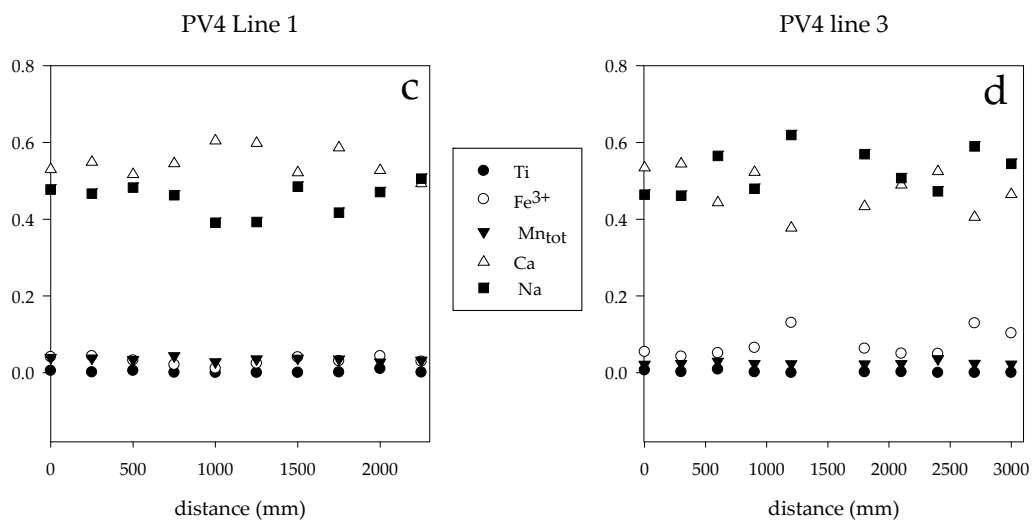


**Figure 5.** Optical microscope (a), BKSE (b) images, (c,d) zoning patterns of different elements (apfu) along two lines of sample PV4.

However, this increase in aegirine component is not related to a notable change in the color; whereas, for example, in sample PV3, high contents of diopside component (86 and 92 mol%, Table 2) correspond to whitish, light-violet-colored areas.

The coexistence both of diopside and omphacite compositions was found only in sample 6, corresponding to lighter and darker gray color in backscattered electron image (Figure 6; analyses 6-1 and 6-2 in Table 2).

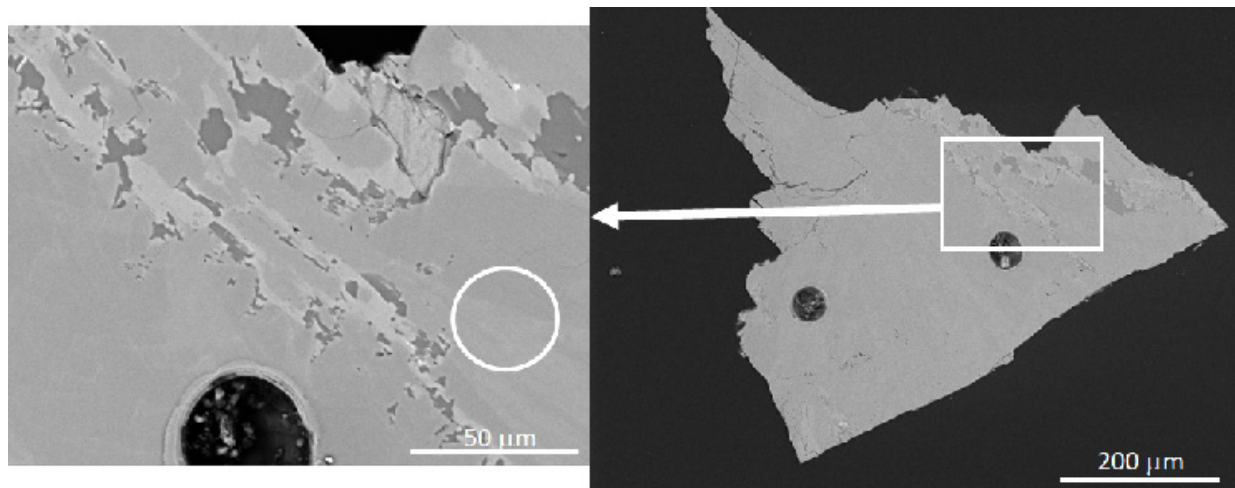


**Figure 6.** BKSE image of sample 6 and enlargement.

The different hues of color observed in the examined samples indeed could be due to the variation of some minor elements such as Mn and Ti; this last will also be discussed in the following together with other trace elements that are notoriously considered responsible for the color change in many minerals. Their content is low both in the massive samples and in the fragments, and the variation of Mn, together with Fe<sup>3+</sup>, is broader than that of Ti. At any rate, a regular variation with the jadeite content does not occur (Figure 7).

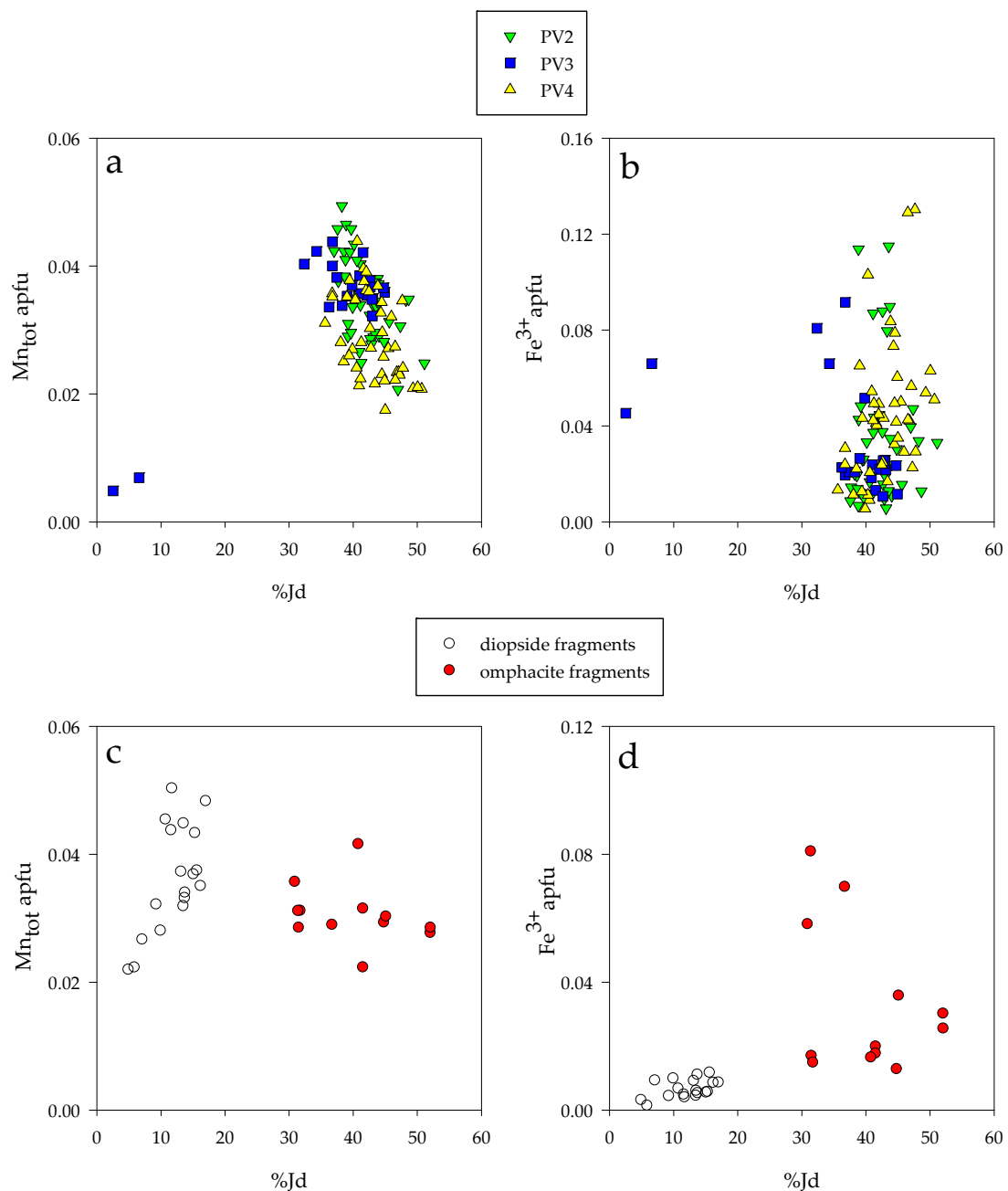


**Figure 7.** Variation of  $Mn_{tot}$  and  $Fe^{3+}$  versus Jadeite mol% (%Jd) in the studied samples. (a)  $Mn_{tot}$  and (b)  $Fe^{3+}$  in massive samples, (c)  $Mn_{tot}$  and (d)  $Fe^{3+}$  in fragments.

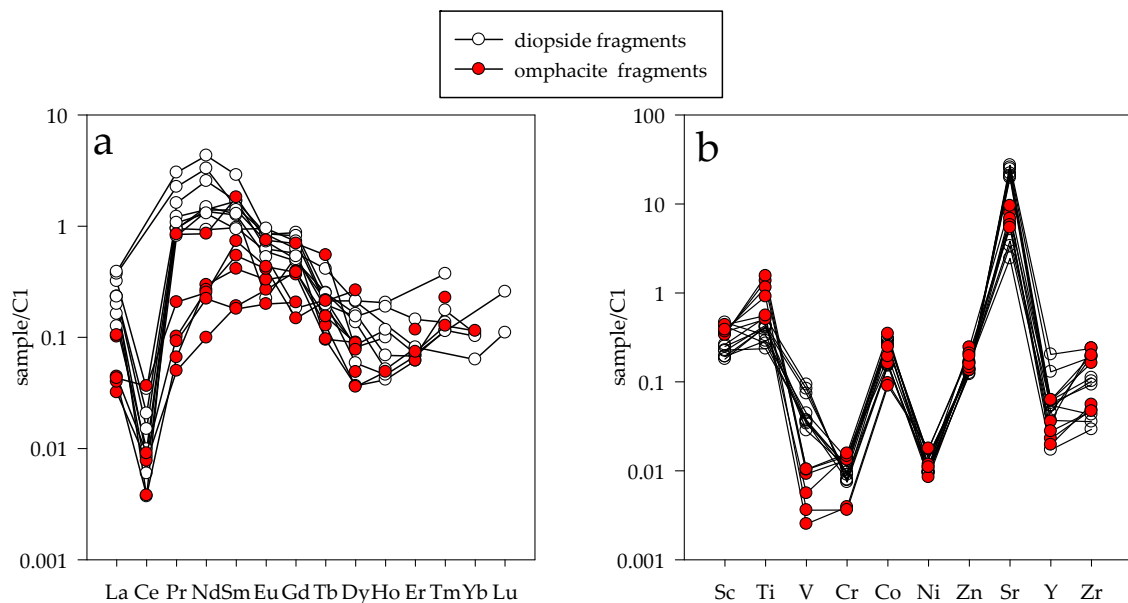
#### 4.3. Trace Elements

REE, Sr, Zr together with trace elements forming the “first transition series” (i.e., Sc, Ti, V, Cr, Co, Ni, and Zn), determined by LA-ICP-MS on the fragments, are reported in Table 3 as average result of single spot analyses and plotted in multi-element diagrams (Figure 8) normalized to the C1 chondrite values [25]. The REE patterns of all the examined samples do not differ significantly and show the typical bell-shaped trend of pyroxenes with a general enrichment in the middle and heavy (MHREE) relative to light (LREE) rare-earth elements. However, omphacites show a REE total content lower than that of diopside samples ( $\Sigma$ REE: 0.20–0.98 vs. 0.88–3.04 ppm) confirming the inverse relationship between REE cation concentration and the jadeite component [26].

**Table 3.** Laser-ablation inductively coupled plasma mass spectroscopy (LA-ICP-MS) analyses of the fragments (average of two points for each fragment, ppm).

Sample	Omphacite Fragments						Diopside Fragments								
	3	4	6	7	12	13	1	2	8	9	10	14	15	16	17
Sc	2.14	2.02	1.98	2.16	2.56	2.26	2.50	2.73	1.55	1.47	1.30	1.33	1.13	1.13	1.06
Ti	219.92	594.32	675.27	501.89	243.09	396.84	117.74	145.46	232.49	175.60	188.48	102.94	179.91	126.15	182.66
V	0.32	0.52	0.58	0.59	0.14	0.21	1.93	2.01	5.30	4.19	4.74	2.09	2.11	2.52	1.61
Cr	39.59	35.32	38.93	41.56	10.38	9.65	31.01	20.80	19.84	23.91	21.24	25.58	29.14	36.18	29.57
Co	82.00	98.18	125.23	175.77	49.16	45.77	150.94	130.86	76.85	78.64	79.56	137.90	151.07	155.34	153.14
Ni	92.84	120.46	128.94	120.57	191.43	195.61	149.35	102.90	103.33	109.76	106.81	105.94	151.69	163.66	164.59
Zn	41.99	45.17	49.06	76.00	65.01	60.97	43.14	38.95	51.13	50.13	52.68	37.84	42.27	43.25	41.65
Sr	47.53	60.98	53.31	74.05	45.24	42.12	171.91	212.75	26.30	19.01	29.88	200.16	161.00	191.97	152.99
Y	0.04	0.05	0.10	0.10	0.03	0.04	0.09	0.31	0.06	0.03	0.08	0.20	0.08	0.10	0.07
Zr	0.31	1.53	1.04	1.27	0.36	0.30	0.60	1.53	0.23	0.19	0.27	1.22	0.65	0.71	1.24
Li	66.39	58.77	84.65	68.84	56.04	53.29	28.28	30.04	18.34	24.66	16.59	24.78	27.70	27.00	31.41
La	0.008	0.009	0.011	0.010	0.024	0.025	0.030	0.076	0.055	0.088	0.092	0.038	0.055	0.047	0.055
Ce	0.005	0.002	0.006	0.023	<	<	0.006	0.021	0.002	<	<	0.004	0.009	0.005	0.013
Pr	0.005	0.006	0.009	0.019	0.008	0.076	0.086	0.110	0.146	0.203	0.273	0.074	0.086	0.085	0.097
Nd	0.046	0.137	0.124	0.117	0.103	0.396	0.429	0.653	1.180	1.530	1.995	0.629	0.645	0.689	0.603
Sm	0.028	0.060	0.078	0.106	0.026	0.262	0.140	0.242	0.243	0.213	0.416	0.182	0.202	0.186	0.135
Eu	0.015	0.018	0.023	0.024	0.011	0.041	0.033	0.034	0.047	0.047	0.047	0.029	0.040	0.012	0.053
Gd	0.078	0.073	0.030	0.077	0.041	0.139	0.097	0.114	0.125	0.174	0.163	0.037	0.100	0.107	0.145
Tb	0.005	0.003	0.008	0.005	<	0.019	0.009	0.015	0.003	0.009	0.007	0.008	0.008	0.006	0.007
Dy	0.009	0.022	0.065	0.022	0.012	0.019	0.034	0.052	0.009	0.040	0.014	0.020	0.053	0.021	0.038
Ho	0.003	<	<	<	<	<	0.003	<	0.002	0.004	0.003	0.006	0.011	0.006	0.010
Er	<	0.010	0.012	0.019	<	<	0.013	0.013	0.010	0.011	0.011	<	<	0.012	0.024
Tm	<	<	0.003	<	<	0.005	<	<	<	0.004	0.003	<	0.008	0.003	0.003
Yb	<	<	0.019	<	<	<	<	0.011	<	0.018	0.017	<	<	<	<
Lu	<	<	<	<	<	<	<	0.003	<	<	<	<	<	0.006	<
ΣREE	0.199	0.341	0.385	0.420	0.225	0.982	0.877	1.342	1.821	2.339	3.040	1.025	1.216	1.185	1.181

&lt; = below the detection limit.

**Figure 8.** C1 normalized rare-earth element (REE) patterns (a) and multi-element diagram (b) abundances of violane fragments.

The inspection of Table 3 indicates that in diopside samples a significant contribution to the total REE budget is given by Nd. All the patterns are also characterized by a noticeable negative Ce anomaly suggesting that its fractionation from the other neighboring REEs developed in oxidizing environment. In fact, REE are typically in the 3<sup>+</sup> oxidation state, but Ce can occur also in the 4<sup>+</sup> oxidation state in changing redox conditions. Therefore, Ce anomaly could be ascribed to the variation of the oxygen chemical potential occurring in the ore of Praborna from the footwall braunite-and violane-rich layer, with prevailing Mn<sup>3+</sup>, to the spessartine bearing Mn<sup>2+</sup>-rich layer of the hanging wall [15]. According to [10], the whole-rocks REE patterns of samples from Praborna ore, showing

the clinopyroxene-braunite-bearing assemblage, display a Ce positive anomaly to which braunite may contribute. It is, therefore, reasonable to suggest that negative and positive Ce anomaly of clinopyroxene and braunite, respectively, tend to compensate each other.

As for REEs, the behavior of the other selected trace elements of omphacite and diopside samples is very similar, and in most cases, the values result  $<1$  in respect to C1 chondritic standard. However, the slight increase in titanium in some omphacites ( $Ti \geq C1$ ) and the significant increase in Sr in all the samples is noteworthy. Thanks to its relatively large ionic radius ( $r = 1.18 \text{ \AA}$ ), strontium is expected to enter the eightfold M2 site of clinopyroxenes [27] where REEs are also hosted [28]. As these last, the Sr content results higher in diopside than in omphacite points confirming the negative correlation between this cation and the jadeite content and showing, as its incorporation in the M2 site is controlled by the charge balance mechanism and promoted by the decrease in the  $Na \rightarrow Ca$  substitution [26,29]. On the contrary, zirconium and the transition elements occupy most commonly the M1 site that can accommodate cations with ionic radii between 0.5 and 1.05  $\text{\AA}$  [30]. Their content is generally low and minor of the C1 value, with the unique exception of Ti that, as noted before, is slightly higher in most omphacites and shows a rough positive correlation with the jadeite component (Figure 9b). On the contrary, vanadium ranges from 0.14 to 0.58 ppm in omphacites and from 1.61 to 5.30 ppm in diopside samples. The content of chromium varies irregularly in all the samples, but the mean values do not differ significantly (29 and 26 ppm in omphacites and diopside samples, respectively). The inspection of Table 3 suggests that both omphacites and diopside samples have appreciable Li content, ranging from 53 to 85 ppm and from 18 to 32 ppm, respectively. Clinopyroxene is the principal carrier of lithium in the eclogitic paragenesis, and its behavior is an important parameter to be considered when assessing the origin and evolution of the whole rocks. On the basis of the results here obtained, the violane from Praborna belongs to the high-Li group clinopyroxenes ( $Li > 8 \text{ ppm}$ ) occurring in eclogite-facies rocks formed at low-T ( $<500 \text{ }^\circ\text{C}$ ) and medium-T ( $550\text{--}900 \text{ }^\circ\text{C}$ ) conditions [31].

The relationship between the chemical variation and the color is more evident from the trace element analyses performed on the little fragments. The comparison of the images of samples shown in Figure 9a, and the data reported in Figure 9b suggest that, as a whole, omphacites, enriched in Ti and Li, show a darker violet hue, while diopside pyroxenes, with a higher content of V and REEs, vary in color from lilac-lavender to light-violet-blue.

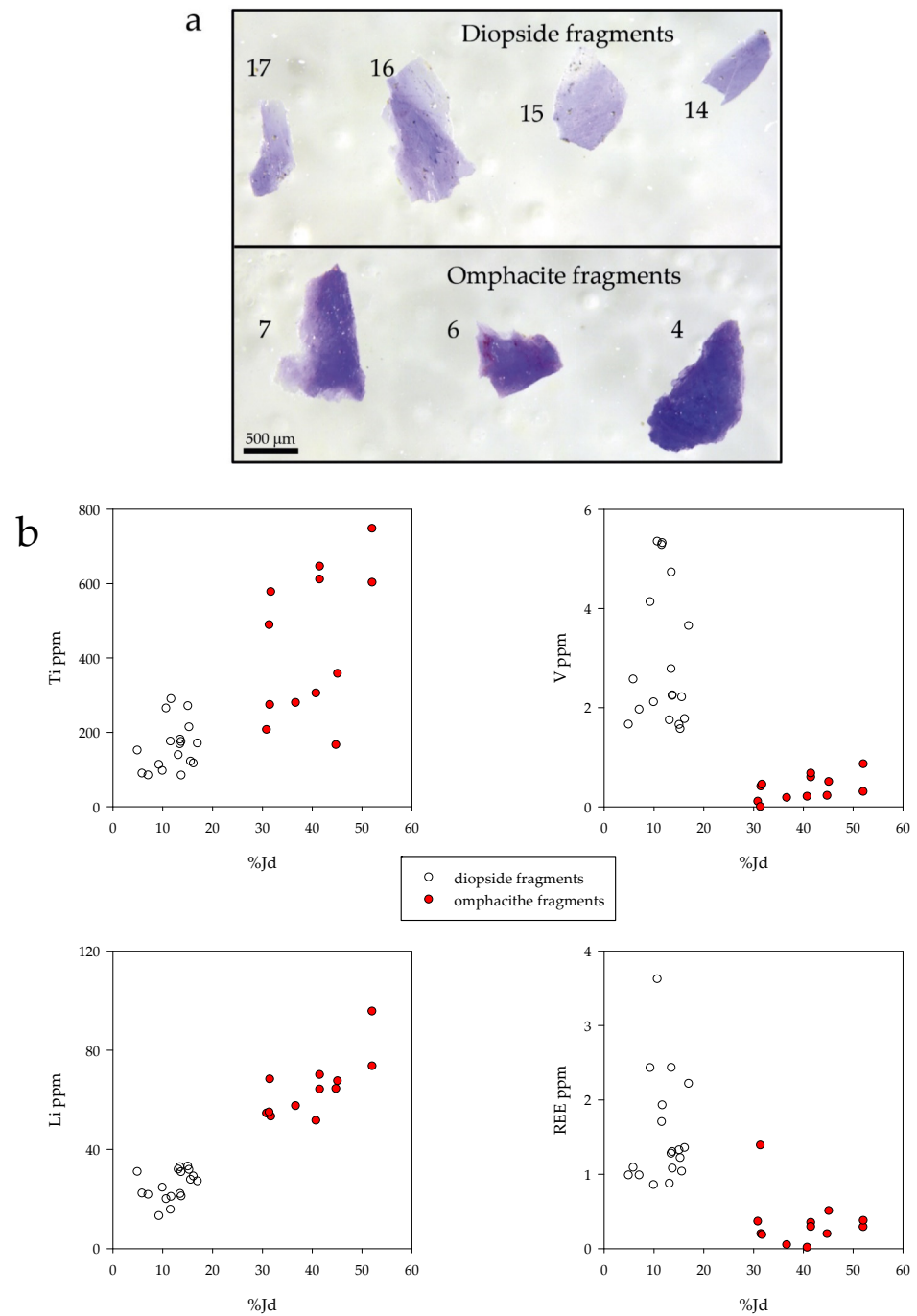


**Figure 9.** Optical microscope images of selected diopside and omphacite fragments (a) and variation of their content of Ti, V, Li, and REE vs. the mole % of the jadeite component (%Jd) (mol%) (b).

#### 4.4. Raman and FTIR Spectroscopy

Figure 10 shows the localization of different area investigated by Raman and FTIR spectroscopy of a representative stone, carved from the same block of gem 2. Raman spectra, from  $100$  to  $1200\text{ cm}^{-1}$ , were performed to distinguish the occurrence and the color of diopside and/or omphacite ([32] and references therein). The minerals associated with the pyroxene resulted albite, calcite, riebeckite, and braunite, as found by optical investigation.

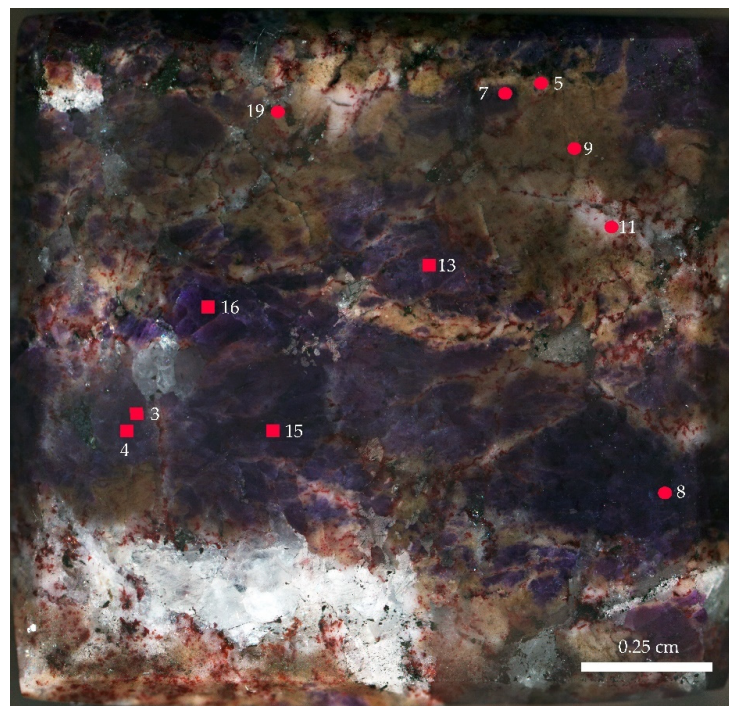


**Figure 10.** Analyzed points by Raman and FTIR spectroscopy. Circles identified diopside and squares omphacite.

The Raman spectra of piroxene silicates are characterized by four types of vibration bands: (1) Si-O nonbridging stretching ( $\text{Si-O}_{\text{nbr}}$ ); (2) Si-O bridging stretching ( $\text{Si-O}_{\text{br}}$ ); (3) O-Si-O bending; (4) cation M1-, M2-oxygen vibration modes (M-O). The stretching modes of  $\text{Si-O}_{\text{nbr}}$  are observed in the spectra at frequencies higher than the modes of  $\text{Si-O}_{\text{br}}$ , due to a stronger force constant, i.e., the coefficient that links the displacement of atoms from their equilibrium position with the force that such displacement induces on adjacent atoms [33–37]. Table 4a,b report the band intensities present in our sample compared with those reported in literature for diopside and omphacite, respectively.

**Table 4.** Raman frequency ( $\text{cm}^{-1}$ ) of our sample and literature data relative to diopside [35,37] (a) and omphacite [37,38] (b).

(a)								Bands
Point 5	Point 6	Point 7	Point 8	Point 9	Point 19	[35]	[37]	
236	225	227	225	226	225	229	230	M-O stretch/bend
256	254	-	267	255	256	255	248	
288	-	-	288	-	264	-	296	
321	328	322	322	325	328	325	323	
367	-	354	354	-	-	359	358	
383	390	388	388	391	393	389	389	
505	503	503	505	509	507	509	507	O-Si-O bend
-	-	527	-	-	527	529	527	
556	557	557	555	560	554	558	558	Si-O <sub>br</sub> stretch
664	665	665	665	666	667	666	665	
-	885	855	859	874	858	854	853	Si-O <sub>nbr</sub> stretch
916	9011	909	906	912	915	-	907	
1010	1011	1010	1010	1013	1013	1010	1010	
1042	1043	1042	1045	1045	1046	1045	1045	

Table 4. Cont.

(b)							
Point 3	Point 4	Point 13	Point 15	Point 16	[37]	[38]	Bands
209	205	206	205	-	223	217	
243	240	249	239	236	248	264	
295	288	290	297	300	296	-	
338	333	330	335	337	327	-	
347	347	-	349	-	356	343	M-O stretch/bend
376	376	389	377	373	389	376	
-	-	-	-	-	451	-	
487	477	478	490	-	480	-	
510	505	507	505	-	506	522	
561	557	-	563	557	563	558	O-Si-O bend
606	-	605	-	-	-	605	
680	680	668	679	679	667	668	
743	747	-	-	-	-	747	Si-O <sub>br</sub> stretch
	864	862	866	-	860	-	
884	887	-	883	-	878	-	
917	912	-	910	-	907	910	Si-O <sub>nbr</sub> stretch
1020	1012	1013	1021	1022	1013	1022	

The spectra assigned to diopside are similar to each other and to those reported in literature [35,37] and characterized by two intense bands, corresponding to the Si-O<sub>nbr</sub> stretching mode at about 1010 cm<sup>-1</sup> and to the stretching of Si-O<sub>br</sub> bonds at 665 cm<sup>-1</sup>. In the 500–560 cm<sup>-1</sup> region, the observed bands were attributed to the O-Si-O bending modes, and in the lower region to the cation–oxygen vibrations. An example is reported in Figure 11a.

The Raman spectra assigned to omphacite are characterized by the stretching modes of Si-O<sub>nbr</sub> with the bands in the region 1012–1022 cm<sup>-1</sup> and the Si-O<sub>br</sub> modes as one or two bands in the range 667–747 cm<sup>-1</sup>. The O-Si-O bending modes are observed in the 500–600 cm<sup>-1</sup> region, and the modes of the interactions between cation and oxygen are located below 500 cm<sup>-1</sup> (an example in Figure 11b).

The difference in the position and intensity of the M-O diopside and omphacite bands is related to the variation of the cation occupancy in the M sites.

Figure 12 presents five representative FTIR reflectance spectra of diopside and omphacite phases identified in the sample. In all the FTIR spectra, the main vibrational bands are localized in the 1200–650 cm<sup>-1</sup> region. In general, no reflectance bands are observed above 1500 cm<sup>-1</sup>, which suggests the absence of OH groups or water molecules in these crystalline phases.

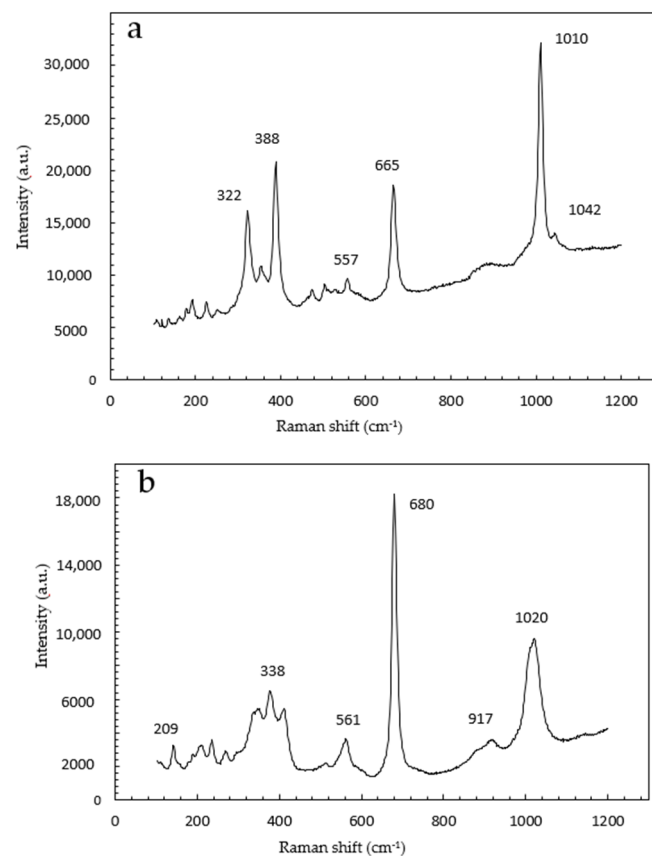


**Figure 11.** Raman spectra of point 7, diopside (a), and point 3, omphacite (b). As it is shown in Figure 10, points presenting violet color, even if with little different hues, correspond both to diopside and omphacite: points 3, 4, 13, 15, and 16 resulted omphacite and points 7 and 8 diopside. Points 5, 11, and 19 with a whitish color resulted diopside.

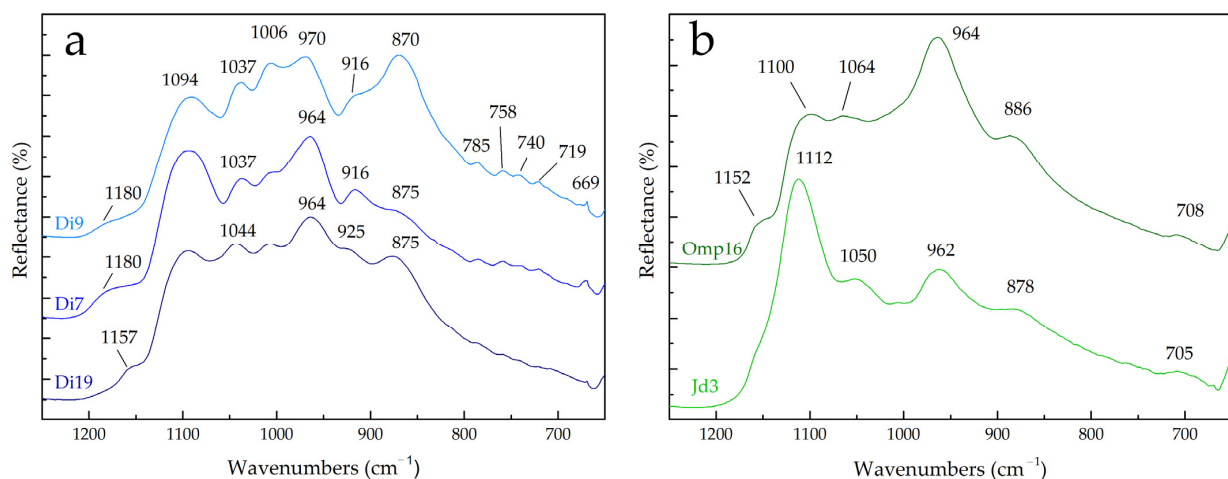


**Figure 12.** FTIR spectra of area 9, 7, and 19 corresponding to diopside (Di) points (a), and FTIR spectra of area 16, 3 corresponding to omphacite (Omp) and Na-rich omphacite (Jd) points (b).

The FTIR reflectance spectra of diopside (Figure 12a) show broad bands at 1094, 1006, and 970–964  $\text{cm}^{-1}$  attributed to the characteristic Si-O stretching modes of the  $\text{SiO}_4$  tetrahedron, while the sharp peak at 669  $\text{cm}^{-1}$  and the other peak at 875–870  $\text{cm}^{-1}$  are assigned to the non-bridging bending vibration of O-Si-O and non-bridging stretching mode of Si-O, respectively [39–41]. All the detected bands are in good agreement with the

vibrations of the functional groups of diopside. However, some differences in terms of relative intensity can be observed among the spectra, and this allows to divide the FTIR patterns in three sub-groups. In particular, in the points 5, 9, the most intense peak of the spectra is at  $870\text{ cm}^{-1}$ ; in the points 7, 11, the two main peaks of FTIR spectra are at  $1094$  and  $964\text{ cm}^{-1}$ ; while in correspondence of point 19, the main band of the vibrational pattern is at  $964\text{ cm}^{-1}$ . These differences could be due to different orientations of diopside crystals within the gem or to variations in the elemental composition of non-stoichiometric diopside phases. The strong reflectance band at  $1044\text{--}1037\text{ cm}^{-1}$  as well as the sequence of weaker peaks at  $785$ ,  $758$ ,  $740$ , and  $719\text{ cm}^{-1}$  in all the FTIR spectra of diopside are due to albite [42], always co-present with diopside in this gem.

The FTIR spectra of omphacite (e.g., in points 13, 16) can be identified by the strong modes at  $964\text{ cm}^{-1}$  ( $\nu$  Si-O) and  $1064\text{ cm}^{-1}$  ( $\nu_{\text{as}}$  Si-O-Si), as well as by the Si-O stretching bands at  $1120$ ,  $1100$ , and  $886\text{ cm}^{-1}$  (Figure 12b) [39,42]. In some omphacitic regions of the sample, e.g., in correspondence of area 3, 4, 15 of the gem, the FTIR spectra display some differences with respect to the FTIR spectrum of omphacite (e.g., pattern Omp16 in Figure 12b). In this second type of spectra (e.g., pattern Jd3 in Figure 12b), the strongest band of the spectrum is at  $1112\text{ cm}^{-1}$  and not at  $964\text{ cm}^{-1}$ . In comparison to omphacite, this band shows a shift at higher wavenumbers ( $1112\text{ cm}^{-1}$  instead of  $1100\text{ cm}^{-1}$ ). In addition, the shoulder band at  $1152\text{ cm}^{-1}$  is less pronounced, and the bands of omphacite initially at  $1064$  and at  $886\text{ cm}^{-1}$  are actually centered at  $1050$  and at  $878\text{ cm}^{-1}$ . Indeed, a similar pattern is in good agreement with the vibrational features (both of position and intensity) of jadeite ( $\text{NaAlSi}_2\text{O}_6$ ) [32,39,43–45]. A similar detection suggests the presence of jadeite in the gem or, most likely, it can be attributed to omphacitic regions where a sodium-enriched omphacite shows compositional variations of the solid solution toward the field of jadeite.

## 5. Discussion and Conclusions

In the literature, there are many papers presenting different hypotheses about blue hues of omphacite/jadeite and diopside gemstones. Dark blue omphacite from Guatemala [46] has a strong compositional zoning (range  $\text{Jd}_{30\text{--}87}\text{Di}_{9\text{--}62}$ ) and contains titanium and iron both as  $\text{Fe}^{2+}$  and  $\text{Fe}^{3+}$  as determined by electron microprobe and Vis-NIR analysis. The Authors attributed the blue, at least in part, to the iron but also to  $\text{Ti}^{4+}$ , which plays a role in the coloration, because the blue color showed a direct relation to titanium content in the analyzed samples. Herd and Peterson [7] studied a violet diopside from Southern Baffin Island, Nunavut, Canada using structural refinement, chemical analysis, and FTIR spectrometry. They suggest that the color is due to intervalence charge-transfer between  $\text{Fe}^{2+}$  and  $\text{Ti}^{4+}$  at the M1 site and owed to the low concentration of Fe in the diopside. They add that  $\text{Mn}^{2+}$  is present in M1 site and that, comparing absorption spectra data,  $\text{Mn}^{3+}$  and  $\text{Fe}^{3+}$  do not contribute to the violet color. More recent papers studying violet diopside from Russia attributed the violet color to the vanadium content [6,47].

“Jade”-like materials were examined using Raman together with UV-Vis-NIR and FTIR absorption spectroscopy and EDXRF analysis by [32] that distinguished “omphacite jade” from “jadeite jade” of green color. LA-ICP-MS analysis of trace elements, combined with UV-Vis spectroscopy, has been recently used to investigate the different color of jadeite with a jadeite content of more than 90% by [48]. The author analyzed jadeites with broad range of colors and found Mn and Cr as responsible for lavender and green colorations, respectively. In a more recent paper on Japanese jadeites of different colors by [49], the lavender color was attributed to a combination of higher Ti and Fe and lower Mn and the blue to the  $\text{Ti}^{4+}\text{-Fe}^{2+}$  charge-transfer. Moreover, trace analyses showed that elements such as Li, B, K, Sr, Ba, and REEs were higher in lavender jadeite than in white and green jadeites from the same locality.

Diopside and omphacite from the mine of Praborna examined in this study are nearly indistinguishable under the microscope, and they show very similar optical properties. The occurrence of omphacite and diopside in the same samples, as well as their textural relationships and compositional variations, has, therefore, been detected only by in situ

chemical or spectroscopic analyses. Regarding the causes of their color, the studies reported so far in the literature have not given a definitive answer.

In the detailed review compiled many years ago [2,4] on samples of violane (both omphacite and diopside), the authors suggested the hypothesis that the main factors controlling the color of this mineral may be manganese, both as  $Mn^{2+}$  and  $Mn^{3+}$ .

The samples examined in this paper display a  $Mn^{3+}$  content, calculated from electron microprobe analyses, ranging from nil to 0.026 apfu, but this variation, as well as that of the  $Mn^{2+}/Mn^{3+}$  ratio, does not appear to have any significant effect on the changing of the blue-violet hue. It is, therefore, reasonable to infer that, in addition to manganese, some other elements may contribute to coloring these stones. Analyses of minor and trace elements, performed by both EMPA and LA-ICP-MS on fragments, suggest that the deeper violet omphacites are characterized by higher Fe, Ti, and Li, whereas higher V and REEs occur in the light blue-violet diopside samples.

Among these last quoted elements, i.e., Fe, Ti, Li, V, and REEs, only Fe, Ti and V are in the group of the transition metals that, together with Mn, Cu, Cr, Co, and Ni, are known as “chromophores” and considered to be the leading cause of color and of color change in minerals. Additionally, REEs (mainly Ce, Pr, Nd) can act as coloring agent, particularly when competing chromophore are absent. This is not the case of lithium that cannot cause the color. As an example, the Li-bearing mica (lepidolite) is colored in lilac to rose-violet or yellow by Mn (mainly  $Mn^{3+}$ ) and  $Fe^{3+}$ , respectively, both substituting for Al in the structure.

Back to violane, the coupled enrichment of titanium and iron in omphacites respect to diopside could have played a significant role on the color characteristics. Such a feature reminds us that, in corundum, the interaction of these two cations implies a charge transfer according to the reaction  $Fe^{2+} + Ti^{4+} \rightarrow Fe^{3+} + Ti^{3+}$  that produces the intense blue colored gem known as sapphire [50]. Moreover, as mentioned above, Abduriyim et al. [49] proved the influence of the charge-transfer between Fe and Ti on the blue color of jadeites from Japan. Alternatively, the change in the oxidation state of iron may have occurred via an intervalence charge transfer  $Fe^{2+} \rightarrow Fe^{3+}$ . This mechanism was proposed as a cause of the violane coloration by [10] on the basis of the study on Chinese “lavender jade” [51]. Whatever process led to the oxidation of iron, it required an increase in the oxygen fugacity that could also explain the fractionation of Ce from the other REEs.

Omphacite and diopside from Praborna mine also differ in the content of vanadium that is considered the main cause of the blue color in the famous tanzanite from Merelani (NE Tanzania), where this cation occurs in trivalent state ( $V^{3+}$ ) as substituting for  $Al^{3+}$  [52]. The light-bluish hue observed in diopside samples could be explained by their enrichment in V with respect to omphacite where the coloring effect of this element could be biased by the higher content of Ti. The ratio between Ti and V results indeed 20 times higher in omphacite than in diopside. In the examined samples, the greatest contribution to REEs budget is given, with the unique exception of omphacite 3, by neodymium. In particular, diopside samples have a Nd content higher than that of omphacites. REEs are occasionally factors in the color of minerals, but it is known in literature that, in the previously mentioned tanzanite, Nd produces an orange to lilac color [53].

In summary, our new data showed that the behavior of minor and trace elements plays a significant role in the color differences of separated diopside and omphacite crystals. However, when the two mineral species are coexisting, as in gemstones and massive samples, they show violet hues indistinguishable to the naked eye and can, therefore, be identified only by in situ chemical or spectroscopic analyses. The bulk of chemical variations observed in these two minerals species, as well as their different crystallographic properties, are related to the complex metamorphic history of the St. Marcel area, and their textural relationship can still be a matter of investigation. At the same time, the scientific debate does not change the interest of violane for gem collectors and jewelers both if it occurs in carved gemstones and in quartz as inclusions.

**Supplementary Materials:** The following are available online at <https://www.mdpi.com/2075-163X/11/2/171/s1>, Table S1: LA-ICP-MS minimum detection limits (99%\_confidence).

**Author Contributions:** Conceptualization and methodology, V.D., R.B., and F.C.; formal analysis, V.D., F.C., N.M., A.L., and E.P.; investigation, V.D., R.B., and F.C.; data curation, V.D.; writing—original draft preparation, V.D., R.B., and F.C.; writing—review and editing, V.D. and R.B. All authors have read and agreed to the published version of the manuscript.

**Funding:** This research received no external funding.

**Institutional Review Board Statement:** Not applicable.

**Informed Consent Statement:** Not applicable.

**Data Availability Statement:** Not applicable.

**Acknowledgments:** We are grateful to Maurizio Scacchetti for lending us some of the gems studied in this work.

**Conflicts of Interest:** The authors declare no conflict of interest.

## References

- Ciriotti, M.E.; Fascio, L.; Pasero, M. *Italian Type Minerals*; Plus: Pisa, Italy, 2009.
- Bondi, M.; Mottana, A.; Kurat, G.; Rossi, G. Cristallochimica del violano e della schefferite di St. Marcel (Valle d’Aosta). *Rend. Soc. It. Min. Petr.* **1978**, *34*, 15–25.
- Brown, P.; Essene, E.J.; Peacor, D.R. The mineralogy and petrology of manganese-rich rocks from St. Marcel, Piedmont, Italy. *Contrib. Mineral. Pet.* **1978**, *67*, 227–232. [\[CrossRef\]](#)
- Mottana, A.; Rossi, G.; Kracher, A.; Kurat, G. Violan revisited: Mn-bearing omphacite and diopside. *Tsch. Miner. Petr. Mitt.* **1979**, *26*, 187–201. [\[CrossRef\]](#)
- Griffin, W.L.; Mottana, A. Crystal chemistry of clinopyroxenes from the St. Marcel manganese deposit, Val d’Aosta, Italy. *Am. Mineral.* **1982**, *67*, 568–586.
- Cara, W.; Laurs, B.M. Blue diopside from Russia. *J. Gemmol.* **2020**, *37*, 124–126.
- Herd, C.D.K.; Peterson, R.C.; Rossman, G.R. Violet-colored diopside from Southern Baffin Island, Nunavut, Canada. *Can. Mineral.* **2000**, *38*, 1193–1199. [\[CrossRef\]](#)
- Reinecke, T. Crystal chemistry and reaction relations of piemontites and thulites from highly oxidized low grade metamorphic rocks at Vitali, Andros Island, Greece. *Contrib. Mineral. Pet.* **1986**, *93*, 56–76. [\[CrossRef\]](#)
- Macrì, M.; Troilo, F.; Serracin, M. A new gemstone from Italy: “A violane quartz”. *Gems Gemol.* **2007**, *43*, 262–263.
- Tumiati, S. Geochemistry, mineralogy and petrology of the eclogitized manganese deposit of Praborna (Valle d’Aosta, Western Italian Alps). Ph.D. Thesis, Università dell’Insubria (Como, Italy)–Université Denis Diderot, Paris, France, 2005. Unpublished.
- Dal Piaz, G.V. La formazione mesozoica dei calcescisti con pietre verdi fra la Valsesia e la Valtouranche ed i suoi rapporti strutturali con il ricoprimento del monte Rosa e con la Zona Sesia-Lanzo. *Boll. Soc. Geol. It.* **1965**, *84*, 67–104.
- Bearth, P. *Die Ophiolite der Zone von Zermatt-Saas Fee. Beitr. Geol. Karte Schweiz*; Kümmerly & Frey: Bern, Switzerland, 1967; NF132.
- Ernst, W.G.; Dal Piaz, G.V. Mineral parageneses of eclogitic rocks and related mafic schists of the Piemonte ophiolite nappe, Breuil-St. Jacques area, Italian Western Alps. *Am. Mineral.* **1978**, *63*, 621–640.
- Martin-Vernizzi, S. La mine de Praborna (Val d’Aoste, Italie): Une Série Manganésifère Métamorphisée Dans le Facies Eclogite. Ph.D. Thesis, Université Pierre et Marie Curie, Paris, France, 1982.
- Tumiati, S.; Martin, S.; Godard, G. Hydrothermal origin of manganese in the high-pressure ophiolite metasediments of Praborna ore deposit (Aosta Valley, Western Alps). *Eur. J. Mineral.* **2010**, *22*, 577–594. [\[CrossRef\]](#)
- Castello, P. Il giacimento di Praborna (S. Marcel-AO). *Riv. Min. It.* **1982**, *3*, 87–92.
- Breithaupt, A. Bestimmung neuer Mineralien. *J. für Prakt. Chem.* **1838**, *15*, 320–338. [\[CrossRef\]](#)
- Des Cloizeaux, A. *Manuel de Minéralogie*; (2 volumes: I, 1862; II, 1874, 19–20); Dunod Éditeur: Paris, France, 1862.
- Schluttig, E. Chemisch-Mineralogische Untersuchungen von weniger bekannten Silicaten. *Zeits. Kryst. Min.* **1888**, *13*, 73–76.
- Hey, M.H. *An Index of Mineral Species and Varieties*; British Museum: London, UK, 1962.
- Tröger, E. *Optische Bestimmung der Gesteinsbildender Minerale*; Teil 2. Schweizerbart’sche Verlagsbuchhandlung: Stuttgart, Germany, 1967.
- Strunz, H. *Mineralogische Tabellen*; Akademische Verlagsgesellschaft, Geest & Portig: Leipzig, Germany, 1970.
- Morimoto, N.; Fabriès, J.; Ferguson, A.K.; Ginzburg, I.V.; Ross, M.; Seifert, F.A.; Zussman, J.; Aoki, K.; Gottardi, G. Nomenclature of pyroxenes. *Miner. Mag.* **1988**, *53*, 535–550. [\[CrossRef\]](#)
- Martin, S.; Rebay, G.; Kienast, J.R.; Mevel, C. An eclogitized oceanic palaeo-hydrothermal field from the St. Marcel Valley (Italian Western Alps). *Ophioliti* **2008**, *33*, 49–63.
- Anders, E.; Grevesse, N. Abundances of the elements: Meteoritic and solar. *Geochim. Cosmochim. Acta* **1989**, *53*, 197–214. [\[CrossRef\]](#)

26. Bocchio, R.; De Capitani, L.; Ottolini, L.; Cella, F. Trace element distribution in eclogites and their clinopyroxene/garnet pair: A case study from Soazza (Switzerland). *Eur. J. Mineral.* **2000**, *12*, 147–161. [[CrossRef](#)]
27. Burt, D.M. Compositional and phase relations among rare earth element minerals. In *Geochemistry and Mineralogy of Rare Earth Elements*; Lipin, B.R., McKay, G.A., Eds.; Reviews in Mineralogy; Mineralogical Society of America: Washington, DC, USA, 1989; Volume 21, pp. 259–307.
28. Oberti, R.; Caporuscio, F.A. Crystal chemistry of clinopyroxenes from mafic eclogites: A study on the key role of the M2 site population by means of crystal-structure refinement. *Am. Mineral.* **1991**, *76*, 1141–1152.
29. Messiga, B.; Tribuzio, R.; Bottazzi, P.; Ottolini, L. An ion microprobe study on trace element composition of clinopyroxenes from blueschist and eclogitized Fe–Tigabbros, Ligurian Alps, northwestern Italy: Some petrologic considerations. *Geochim. Cosmochim. Acta* **1995**, *59*, 59–75.
30. Meagher, E.P. Silicate Garnets. In *Orthosilicates*; Ribbe, P.H., Ed.; Reviews in Mineralogy; Mineralogical Soc. of America: Washington, DC, USA, 1980; Volume 5, pp. 25–66.
31. Woodland, A.B.; Seitz, H.-M.; Altherr, R.; Marschall, H.; Olker, B.; Ludwig, T. Li abundances in eclogite minerals: A clue to a crustal or mantle origin? *Contrib. Mineral. Pet.* **2002**, *43*, 587–601. [[CrossRef](#)]
32. Coccato, A.; Karampelas, S.; Wörle, M.; van Willigen, S.; Pétrequin, P. Gem quality and archeological green ‘jadeite jade’ versus ‘omphacite jade’. *J. Raman Spectr.* **2014**, *45*, 1260–1265. [[CrossRef](#)]
33. McMillan, P. Structural studies of silicate glasses and melts-applications and limitations of Raman spectroscopy. *Am. Mineral.* **1984**, *69*, 622–644.
34. Mernagh, T.P.; Hoatson, D.M. Raman Spectroscopic Study of Pyroxene Structures from the Munni Munni Layered Intrusion, Western Australia. *J. Raman Spectr.* **1997**, *28*, 647–658. [[CrossRef](#)]
35. Huang, E.; Chen, C.H.; Huang, T.; Lin, E.H.; Xu, J. Raman spectroscopic characteristics of Mg-Fe-Ca pyroxenes. *Am. Mineral.* **2000**, *85*, 473–479. [[CrossRef](#)]
36. Katerinopoulou, A.; Musso, M.; Amthauer, G. A Raman spectroscopic study of the phase transition in omphacite. *Vib. Spectr.* **2008**, *48*, 163–167. [[CrossRef](#)]
37. Buzatu, A.; Buzgar, N. The Raman study of single-chain silicates. In *Analele Științifice Ale Universitatii, Al. I. Cuza” IAȘI Geologie; “Al. I. Cuza” University of Iași*; Iași, Romania, 2010; pp. 1429–1443.
38. Downs, R.T. The RRUFF Project: An integrated study of the chemistry, crystallography, Raman and infrared spectroscopy of minerals. In Proceedings of the Program and Abstracts of the 19th General Meeting of the International Mineralogical Association Kobe, Japan, Commission on Ore Mineralogy, Report of the Sulfosalt Subcommittee, Kobe, Japan, 23–28 July 2006.
39. Ostrooumov, M.; Lasnier, B.; Lefrant, S.; Fritsch, E. FT-Raman and infrared reflexion spectrometry of minerals and gems. Available online: <http://www.geocities.ws/ostrooum/> (accessed on 7 January 2021).
40. Jafari Baghjeghaz, M.; Salahinejad, E. Enhanced sinterability and in vitro bioactivity of diopside through fluoride doping. *Ceram. Int.* **2017**, *43*, 4680–4686. [[CrossRef](#)]
41. Shahrouzifar, M.R.; Salahinejad, E. Strontium doping into diopside tissue engineering scaffolds. *Ceram. Int.* **2019**, *45*, 10176–10181. [[CrossRef](#)]
42. Manrique-Ortega, M.D.; Mitrani, A.; Casanova-González, E.; Jiménez-Galindo, L.A.; Ruvalcaba-Sil, J.L. Methodology for the non-destructive characterization of jadeite-jade for archaeological studies. *Spectrochim. Acta A* **2019**, *217*, 294–309. [[CrossRef](#)]
43. Ou Yang, C.M.; Jian, Q.L.; Hansheng, L.; Kwok, B. Recent studies on inky black omphacite jade. *J. Gemmol.* **2003**, *28*, 337.
44. Franz, L.; Tay, T.S.; Hänni, H.A.; de Capitani, C.; Thanasuthipitak, T.; Atichat, W. A Comparative Study of Jadeite, Omphacite and Kosmochlor Jades from Myanmar, and Suggestions for a Practical Nomenclature. *Gems Gemol.* **2014**, *34*, 2010–2229. [[CrossRef](#)]
45. Zhao, L.; Ma, H.; Fang, C.; Ding, L.; Jia, X. Synthesis and characterization of purple NaAlSi<sub>2</sub>O<sub>6</sub> jadeite under high pressure and high temperature. *J. Cryst. Growth* **2018**, *499*, 30–34. [[CrossRef](#)]
46. Harlow, G.E.; Quin, E.P.; Rossman, G.R.; Rohtert, W.R. Blue omphacite from Guatemala. *Gems Gemol.* **2004**, *40*, 68–70.
47. Simakin, A.G.; Kislav, E.V.; Salova, T.P.; Shaposhnikova, O.Y.; Nekrasov, A.N. Reduced CO<sub>2</sub> fluid as an agent of ole-forming processes: A case study of dolomite-replacement skarns at the Yoko-Dovyren massif. *Petrology* **2019**, *27*, 1–16. [[CrossRef](#)]
48. Lu, R. Color origin of lavender jadeite: An alternative approach. *Gems Gemol.* **2012**, *48*, 273–283. [[CrossRef](#)]
49. Abduriyim, A.; Saruwatari, K.; Katsurada, Y. Japanese jadeite: History, characteristics, and comparison with other sources. *Gems Gemol.* **2017**, *53*, 48–67. [[CrossRef](#)]
50. Bristow, J.K.; Parker, S.C.; Catlow, C.R.A.; Woodley, S.M.; Walsh, A. Microscopic origin of the optical processes in the blue sapphire. *Chem. Commun.* **2013**, *49*, 5259–5261. [[CrossRef](#)]
51. Rossman, G.R. Lavender jade: The optical spectrum of Fe<sup>3+</sup> and Fe<sup>2+</sup>-Fe<sup>3+</sup> inter-valence charge transfer in jadeite from Burna. *Am. Mineral.* **1974**, *59*, 868–870.
52. Bocchio, R.; Adamo, I.; Bordoni, V.; Caucia, F.; Diella, V. Gem-quality zoisite from Merelani (Northwestern Tanzania): Review and new data. *Per. Mineral.* **2012**, *81*, 379–391. [[CrossRef](#)]
53. Olivier, B. The Geology and Petrology of the Merelani Tanzanite Deposit, N.E. Tanzania. Ph.D. Thesis, Stellenbosch University, Stellenbosch, South Africa, 2006.